communications physics

Article

https://doi.org/10.1038/s42005-024-01855-8

Environment induced dynamical quantum phase transitions in two-qubit Rabi model

Grazia Di Bello [1] ✉, Andrea Ponticelli[1,2], Fabrizio Pavan[1], Vittorio Cataudella[2,3], Giulio De Filippis[2,3], Antonio de Candia[2,3] & Carmine Antonio Perroni[2,3]

Quantum states beyond thermodynamic equilibrium represent fascinating and cutting-edge research. However, the behavior of dynamical quantum phase transitions in complex open quantum systems remains poorly understood. Here, using state-of-the-art numerical approaches, we show that by quenching the qubits-oscillator coupling in a dissipative two-qubit Rabi model, the system undergoes dynamical quantum phase transitions. These transitions are characterized by kinks in the Loschmidt echo rate function at parameter values close to a thermodynamic quantum phase transition and are associated with distinct entanglement features. The two classes of critical phenomena depend on qubit interactions and entanglement, revealing different behaviors of the critical exponent of the first kink of the Loschmidt echo for interacting versus non-interacting qubits. This research enhances our understanding of non-equilibrium quantum systems and offers potential applications in quantum sensing and metrology, as it examines how dynamical transitions can enhance the sensitivity of the Loschmidt echo to the quench parameters.

One of the most challenging open problems in modern physics is the characterization of the transitions between different quantum phases. In recent decades, the importance of quantum phase transitions (QPTs) has grown considerably in various respects[1]. In general, QPTs are studied by examining long-term dynamics, asymptotic behavior of observables, or the non-analytical behavior of thermodynamic observables and correlators, which can be either local or non-local. The theory of QPTs offers insight into properties at thermodynamic equilibrium, leading to extensive research on phase transitions in quantum many-body systems far from equilibrium[2,3]. The fundamental concept of manipulating a control parameter to induce transitions between different phases has also extended to include open systems[4,5].

Both theoretical studies and experimental observations have focused on a different type of quantum phase transitions that occur on intermediate time scales, known as dynamical quantum phase transitions (DQPTs)[6–9]. In this context, specific quantities exhibit non-analytical behavior over time, where time itself acts as the primary driving parameter for this transition. DQPTs have been analyzed in various closed models, showing the emergence of singularities of the Loschmidt echo at the thermodynamic limit[7]. In general, it is not guaranteed that an equilibrium QPT gives rise to a related non-equilibrium DQPT if the quench of some model parameters is made at initial time. More recently, DQPTs have been also found in models with only a few degrees of freedom, such as the closed quantum Rabi model when the oscillator frequency approaches zero[10].

At the same time, DQPTs have been also investigated in open systems, where the role of the Loschmidt echo is played by the fidelity of the subsystem density matrix operator at finite time with that at initial time[11–13]. Also for such open systems DQPTs have been found in models with many degrees of freedom in the thermodynamic limit[11] and with a few degrees of freedom with respect to different quench parameters[14]. In both cases the environment is treated at weak-coupling Lindblad level and does not actively trigger the phase transition, that is the QPT is already present in the closed system. For such complex systems, additional and more detailed investigations, making use of concepts from quantum information theory[15–17] are imperative to discover the active meaning of entanglement in both QPTs[18] and DQPTs[19].

Recently, a study of the universality laws for DQPT has been proposed[20], focusing on computing the critical exponent of the Loschmidt echo rate function. For nearest neighbors Ising chains, a linear behavior with a critical exponent of 1 has been observed. It is known that long-range interactions characterized by a $1/r^{\gamma}$ behavior ($\gamma \leq 2$) can lead to a DQPT[21], although the precise value of the critical exponent remains unclear. More importantly, in long-range interacting Ising models, the various observed DQPTs are not directly related to the underlying equilibrium phase transition[7]. Furthermore, other studies[22,23] have demonstrated that introducing random interactions in an Ising model or tuning the quench parameters can lead to a reduction of the critical exponent from its expected integer value of 1 to small non-integer values.

[1]Dip. di Fisica E. Pancini, Università di Napoli Federico II, Napoli, Italy. [2]INFN, Sezione di Napoli, Complesso Universitario di Monte S. Angelo, Napoli, Italy. [3]SPIN-CNR and Dip. di Fisica E. Pancini, Università di Napoli Federico II, Napoli, Italy. ✉e-mail: grazia.dibello@unina.it

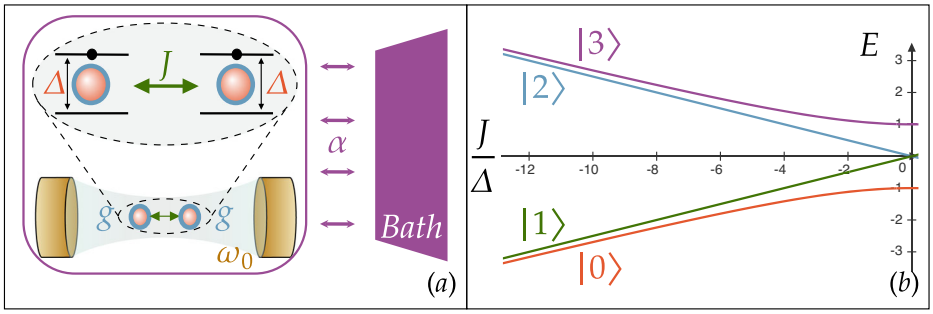

Fig. 1 | Two-qubit dissipative Rabi model and closed system energy diagram. Model described by the Hamiltonians in Eqs. (1) and (2) (**a**): two qubits with energy gap Δ interacting through J and connected to an oscillator through g. The cavity housing the qubits is in contact with an Ohmic bath through α. Energy spectrum (in units of Δ) of the system consisting of the two interacting qubits (**b**), as a function of the ratio J/Δ in the ferromagnetic region (negative values of $\frac{J}{\Delta}$ on x-axis).

We also emphasize that dynamical transitions have garnered significant interest due to their sensitivity to parameter changes over time, not just at infinite times. This sensitivity can be relevant to quantum sensing, as highlighted by recent studies. It is known that quantum criticality can enhance quantum sensing capabilities[24]. This phenomenon has been studied in closed systems like the Jaynes-Cummings model[25] and the quantum Rabi model[26], and recently in some open quantum systems[27]. It has also been proved experimentally[28] in a non-equilibrium Rydberg atomic gas that many-body critical enhanced metrology can be achieved for sensing external microwave electric fields. Our study explores a similar criticality-enhanced sensitivity of the Loschmidt echo in the presence of DQPTs in many-body systems, which are promising resources for sensing and metrology applications.

In this article, we analyze a dissipative two-qubit Rabi model, where two interacting qubits are coupled to an oscillator that interacts with an Ohmic bath (see Fig. 1a).

Since no analytical solution exists to compute the time-dependent behavior of the system and its Loschmidt echo, including multiple bath degrees of freedom, we apply the time-dependent variational principle (TDVP) with a matrix product state (MPS) ansatz, performing a quench on the qubit-oscillator coupling constant. We first investigate the system thermodynamic properties using the worldline quantum Monte Carlo (WLMC) method to compute mean values and correlation functions at imaginary times. We also use density-matrix renormalization group (DMRG) to compute the ground state of the Hamiltonian as an MPS. Our study characterizes the system QPT through the bimodal magnetization distribution and qubits entanglement properties. Additionally, we explore short- and long-range interactions in the classical Ising spin chains obtained via the path integral formalism.

We show that DQPTs reflect key features of QPTs under non-equilibrium conditions, with singularities in the rate function emerging similarly to those in integrable systems[6–9], particularly at qubit-oscillator coupling values near QPTs. We further examine DQPT universality, identifying two distinct classes for the critical exponent of the Loschmidt echo rate function, contrasting with equilibrium QPTs. Significant differences in behavior arise based on whether the qubits interact ferromagnetically, highlighting the role of interactions and entanglement.

Results

Dissipative quantum Rabi model with two interacting qubits

We consider two interacting qubits connected through a harmonic oscillator to an Ohmic bath[16] (see Fig. 1a). In a related study[29], we explored the effects of changing the spectral density of the bath from Ohmic to sub-Ohmic and super-Ohmic. We set $\hbar = k_B = 1$ and the Hamiltonian that describes the system is given by: $H = H_S + H_B + H_{S-B}$. Here, the system (qubits and oscillator) energy H_S is defined as:

$$H_S = -\frac{\Delta}{2}\left(\sigma_x^1 + \sigma_x^2\right) + \frac{J}{4}\sigma_z^1\sigma_z^2 + \omega_0 a^\dagger a + g(a + a^\dagger)\left(\sigma_z^1 + \sigma_z^2\right), \quad (1)$$

where Δ is the frequency of the two qubits, J is the strength of the interaction between them, and σ_i^j (with $i = x, y, z$ and $j = 1, 2$) are the Pauli matrices. The oscillator frequency is ω_0, and a ($a^\dagger$) are the annihilation (creation) operators. The parameter g represents the coupling strength between the qubits and the oscillator. We emphasize that there should be a self-interaction, dipole-dipole term between the qubits which ensures an exact cancellation at zero frequency with the cavity-mediated interaction, as expected from gauge invariance[30]. This term is proportional to $S_z^2 = (\sigma_z^1 + \sigma_z^2)/4$. By expanding this square, we obtain two terms proportional to the identity operator on the two-qubit system, and the last term takes the form $\frac{g^2}{2\omega_0}\sigma_z^1\sigma_z^2$. This can be interpreted as an additional interaction between the two qubits due to the presence of the cavity. In this context, our J in Equation (1) represents an effective interaction that also accounts for this additional term.

The bath Hamiltonian and its interaction with the system are given by:

$$H_B + H_{S-B} = \sum_{i=1}^{N}\left[\frac{p_i^2}{2M_i} + \frac{k_i}{2}(x_0 - x_i)^2\right]. \quad (2)$$

The bath is represented as a collection of N oscillators with frequencies $\omega_i = \sqrt{\frac{k_i}{M_i}}$, and coordinates and momenta are denoted by x_i and p_i, respectively. Additionally, x_0 denotes the position operator of the resonator with mass m: $x_0 = \sqrt{\frac{1}{2m\omega_0}}(a + a^\dagger)$. This interaction with the bath describes dissipation as proposed by Caldeira-Leggett[31,32]. The key challenge for implementing our model is to reach our regime of very strong coupling. There are experimental platforms where this parameter regime can be obtained[33]. One relevant possibility is a flux qubit ultrastrongly coupled to a dissipative resonator[34–37]. This system is useful for describing the regime beyond strong coupling. A dissipative resonator can be conceptualized as an oscillator coupled to a bath, imparting a finite decay time and other effects if the coupling is strong. Hence, in our model, we connect the oscillator to an Ohmic bath. In[5], we proposed realizing this model by adding a series of resistors to a flux qubit interacting with its resonator in Figures 6 and 7 of Supplemental Material.

The coupling to the bath induces renormalization effects on several parameters: the oscillator frequency $\bar{\omega}_0$, as well as the interaction strengths $\bar{g}$ and $\bar{g}_i$ (further detailed in Methods Sec. Time-dependent variational principle numerical simulations). This results in the following bath spectral density $J(\omega) = \sum_{i=1}^{N}\frac{k_i\omega_i}{4m\bar{\omega}_0}\delta(\omega - \omega_i) = \frac{\alpha}{2}\omega f\left(\frac{\omega}{\omega_c}\right)$ where α controls the system-bath coupling. Here $f\left(\frac{\omega}{\omega_c}\right)$ is a function that depends on the cutoff frequency for the bath modes, ω_c, which governs the behavior of the spectral density at high frequencies. This function is taken as $f\left(\frac{\omega}{\omega_c}\right) = \Theta\left(\frac{\omega_c}{\omega} - 1\right)$, where $\Theta(x)$ is the Heaviside step function. The cutoff frequency is typically chosen to be the largest energy scale in the system. In the following we set: $\omega_0 = \Delta$, $J = -10\Delta$ (ferromagnetic interaction) and $J = 0$ (antiferromagnetic interaction), $\alpha = 0.1$, $\omega_c = 30\Delta$.

It is worth noticing that the system can be mapped to an equivalent model of two interacting qubits in contact, through σ_z, with a structured bath

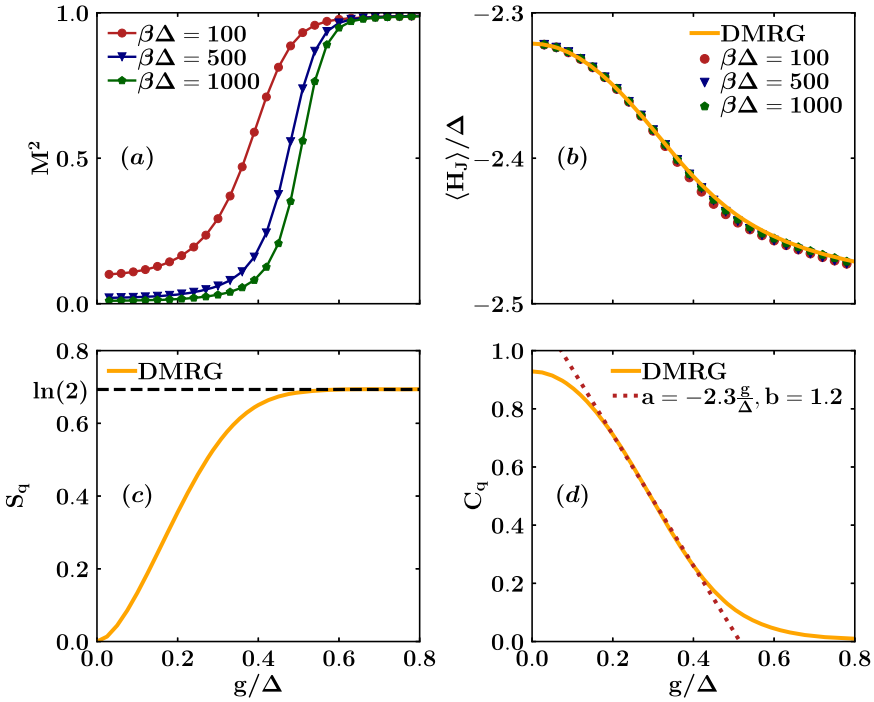

Fig. 2 | Order parameter crossover and entanglement signatures of QPT at thermodynamic equilibrium. Qubits' squared magnetization M^2 (**a**), interaction energy between the qubits $\langle H_J\rangle/\Delta$ (**b**), von Neumann entropy S_q (**c**) and concurrence C_q (**d**) as functions of g/Δ for $J = -10\Delta$, computed through WLMC and DMRG. For the WLMC method the calculations are made for $\beta\Delta \in [100, 1000]$. In panel (**c**), the dashed line represents the maximum von Neumann entropy for a single qubit. In panel (**d**), the dotted line indicates a linear fit of the concurrence performed near the transition, which intersects the g-axis at approximately the critical value.

whose spectral density shows a peak at the oscillator frequency[5,38] (see Equation (5)). The spectrum of the two-qubit Hamiltonian, $H_{qub} = H_S(g = 0)$, is shown in Fig. 1b.

QPT evidences at thermodynamic equilibrium

We first investigate the equilibrium properties of the system, using two different approaches. The first method is the WLMC approach, which is based on path integrals[5,29,39] (see Methods Sec. Worldline Monte Carlo method). Here, the structured bath degrees of freedom are eliminated, resulting in an effective Euclidean action[5,32,40,41], with the kernel expressed in terms of the structured spectral density $J(\omega)$. This structure is characteristic of a spin-boson model but is now extended to involve two qubits interacting with the bath, as outlined in[34,38] (see Methods Sec. Time-dependent variational principle numerical simulations). This transformation leads to a classical system of spin variables distributed along two chains, each of them with length $\beta = 1/T$. The spins experience long-range ferromagnetic interactions both within each chain and between the two chains. The functional integral is computed using a Poissonian measure and adopts a hybrid algorithm[40,42], based on an alternation of Wolff's[43] and Metropolis moves. We find that, as ω_0 remains constant and β tends toward infinity, the kernel displays a power asymptotic behavior, $K(\tau) \simeq 1/\tau^2$. This power-law behavior with an exponent of 2 determines the onset of a Beretzinski-Kosterlitz-Thouless (BKT) QPT. In the Supplementary Note 1 we perform a BKT scaling for a parameter regime that allows for feasible numerical analysis and confirm that the nature of the transitions is indeed BKT (see Supplementary Fig. 1) for the other parameter regimes analyzed in the paper, as they belong to the same universality class. In this respect, another interesting experimental challenge could be the possibility of observing the interplay between short-range and long-range interactions in relation to DQPTs.

The second method we employ is the DMRG (see Methods Sec. Density-matrix renormalization group algorithm), an adaptive algorithm for computing eigenstates of many-body Hamiltonians. It is particularly effective for calculating low-energy properties of one-dimensional and two-dimensional quantum systems. DMRG uses the MPS representation to determine the ground state of low-dimensional quantum systems. In particular, we use the ITensor library[44] for a system with a bath of $N = 300$ harmonic oscillators.

Squared magnetization, interaction energy, and entanglement

In Fig. 2a, we present the squared magnetization of the qubits, defined as $M^2 = \frac{1}{4\beta}\int_0^\beta d\tau\langle(\sigma_z^1 + \sigma_z^2)(\tau)(\sigma_z^1 + \sigma_z^2)(0)\rangle$, where τ labels the positions of the spins on the two equivalent chains (corresponding to the two spins labeled by the superscripts ^{1} and ^{2}), after eliminating the bath degrees of freedom in favour of an effective classical system of spins as discussed in ref. 34 (see Methods Sec. Worldline Monte Carlo method). We plot this magnetization as a function of g/Δ for three different inverse temperatures, $\beta\Delta = \{100, 500, 1000\}$. The data obtained using WLMC method exhibit a crossover for M^2 from 0 to 1 increasing g/Δ that becomes sharper and sharper lowering the temperature. This behavior suggests the occurrence of the BKT QPT, which is estimated to set in at a critical value of $g_c \approx 0.5\Delta$ from $\beta\Delta = 10^3$ data. Additionally, we calculate the mean value of the interaction Hamiltonian between the two qubits, denoted as $\langle H_J\rangle = J\langle\sigma_z^1\sigma_z^2\rangle/4$, as a function of g/Δ for the same three temperature values (see Fig. 2b). We emphasize that both the WLMC and DMRG methods yield consistent results. Note that the interaction becomes more negative with increasing values of g since the bath induces an effective ferromagnetic coupling between the spins.

To analyze the entanglement properties of the system in the presence of the QPT, we determine the qubits' density operator ρ_q and compute the qubits' entropy, denoted as $S_q = -\mathrm{Tr}\{\rho_q \ln \rho_q\}$, and the concurrence, given by $C_q = \max(0, \lambda_1 - \lambda_2 - \lambda_3 - \lambda_4)$. Here, λ_i represents the eigenvalues of the Hermitian matrix $\sqrt{\sqrt{\rho_q}\tilde{\rho}_q\sqrt{\rho_q}}$, and $\tilde{\rho}_q = (\sigma_y^1 \otimes \sigma_y^2)\rho_q^*(\sigma_y^1 \otimes \sigma_y^2)$, with * indicating complex conjugation. In Fig. 2c, d, we present the entropy and entanglement as functions of g/Δ, computed using the DMRG algorithm. The entropy increases for values of g near the critical point, approaching a value of approximately ln(2) just at the critical values determined by the WLMC approach. We also notice the similarity between Fig. 2a, c. In contrast, as shown in Fig. 2d, the concurrence decreases as a function of g, approaching zero. Moreover, through a linear fit of the concurrence within the critical region ($C_q = ag/\Delta + b$ in Fig. 2d), it becomes evident that the line intersects the g-axis at approximately $g \approx 0.5\Delta$, a value close to the estimated critical point. This behavior can be explained by the qubits approaching a two-degenerate state at the BKT QPT, where they are either both in the "up"

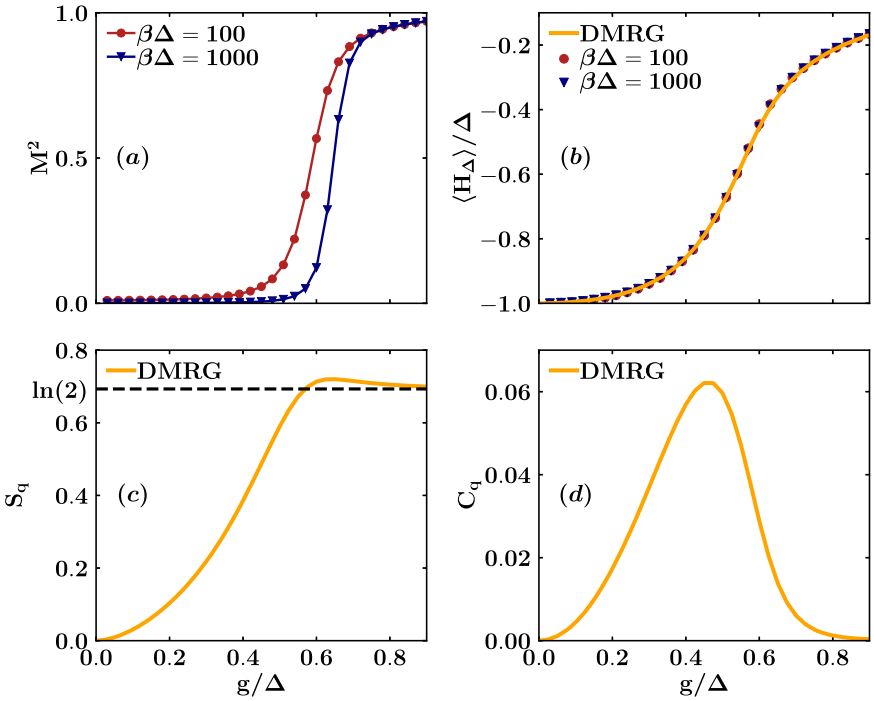

Fig. 3 | Order parameter crossover and entanglement signatures of QPT at thermodynamic equilibrium. Qubits' squared magnetization M^2 (**a**), qubits' energy $\langle H_\Delta \rangle/\Delta$ (**b**), von Neumann entropy S_q (**c**) and concurrence C_q (**d**) as functions of g/Δ for $J = 0$, computed through WLMC and DMRG. For the WLMC method the calculations are made for $\beta\Delta \in [100, 1000]$. In panel (**c**), the dashed line represents the maximum von Neumann entropy for a single qubit.

or "down" state. This clearly results from a lack of entanglement between the two qubits and an enhancement of entanglement of each of them with the bath[39].

Now we conduct the same analysis at thermodynamic equilibrium for the case of zero interaction J between the two qubits. Here, we demonstrate the agreement in thermodynamic quantities computed through both DMRG and WLMC methods. Figure 3a presents the squared magnetization of the qubits (M^2), plotted as a function of g/Δ for two different inverse temperatures, $\beta\Delta = 100$ and $\beta\Delta = 1000$. With the WLMC method, we observe a crossover for the squared magnetization from 0 to 1 around a critical value of $g_c \approx 0.6\Delta$. This jump becomes more pronounced as the temperature decreases. Furthermore, we calculate the mean value of the qubits Hamiltonian, denoted as $\langle H_\Delta \rangle = -\Delta\langle \sigma_x^1 + \sigma_x^2 \rangle/2$, as a function of g/Δ for the same two temperature values (see Fig. 3b). Both the WLMC and DMRG methods yield consistent results. The qubits Hamiltonian does not exhibit a jump but becomes less negative as the bath reduces the effective qubits gap with increasing values of g.

Figure 3c, d present the entropy and entanglement as functions of g/Δ. The entropy increases for values of g near the critical point, asymptotically approaching a value of approximately ln(2). Conversely, the concurrence is almost zero everywhere, except for a small peak near the transition. Again this behavior is consistent with the qubits approaching a two-degenerate state near the transition. The difference from the case of non-zero J is that the concurrence does not change much because the qubits prefer to entangle with the bath to facilitate the transition and entropy can be slightly greater than ln(2).

Magnetization distribution and correlations

Since M^2 displays a crossover from 0 to 1 (Fig. 2a), one naturally wonders if this is related to the onset of a BKT QPT. This question can be better addressed studying the distribution of the normalized magnetization, denoted as $P(M/2)$. In Fig. 4, we plot the magnetization distribution for two different values of g/Δ, smaller and larger of the estimated one for BKT transition. When $g = 0.21\Delta < g_c$ (Fig. 4a), the distribution exhibits a single peak centered at $M = 0$. On the other hand, for $g = 0.66\Delta > g_c$ (Fig. 4c), it acquires a bimodal character, with two peaks centered at $M/2 = \pm 1$, again with the same vanishing mean value. We emphasize that, above g_c, the distribution develops two peaks that are expected to become two delta functions, centered at $\pm\sqrt{M^2}$, in the thermodynamic limit. It's also worth noting that the formation of a bimodal distribution is clearly related to the crossover observed in M^2. This behavior, reminiscent of classical thermodynamics, signals the emergence of a QPT. In addition, we can examine the correlations $C(\tau) = \langle (\sigma_z^1 + \sigma_z^2)(\tau)(\sigma_z^1 + \sigma_z^2)(0) \rangle$ as another indicator of the occurrence of the QPT. Figure 4 shows the distinct behavior before and after the onset of the transition. Specifically, the normalized correlation function, defined as $C = C(\tau/(\beta/2))/C(0)$, tends toward 0 as τ approaches $\beta/2$ before the critical point (Fig. 4b) and converges to a finite value, i.e., M^2, after the transition (Fig. 4d), indicating the long-range nature of the correlations between the spins above g_c.

Dynamics of energy and entanglement

We investigate the out-of-equilibrium properties of the system, focusing on the behavior of energy and entanglement over time. To accomplish this, we employ the TDVP algorithm[45–47] (see Methods Sec. Time-dependent variational principle numerical simulations), implemented using the ITensor library[44], to evolve the wavefunction of the entire system represented as an MPS. The adoption of this technique proves advantageous for our system strongly coupled to the environment, enabling us to achieve long simulation times. Consequently, we can compare these behaviors with those computed using the DMRG at thermodynamic equilibrium. Specifically, we choose the ground state of the Hamiltonian $H_S(g = 0)$ (state $|0\rangle$ in Fig. 1) as the initial state for simulations and calculate the qubits' von Neumann entropy $S_q(t)$, the concurrence $C_q(t)$, and the mean values of the various contributions to the total energy of the system, including $\langle H_S(t) \rangle$, $\langle H_B(t) \rangle$, and $\langle H_{S-B}(t) \rangle$ for different values of g, crossing the critical point. Figure 5a, b demonstrate that both entropy and concurrence are approaching thermodynamic values. Moreover, the greater g, the less time the system needs to reach the equilibrium values.

We stress that from a dynamical point of view, this model also exhibits a delocalized-localized transition. In the Rabi model, this localization physically manifests as a reduction to a sort of two-level system for the two qubits that can only be found in one of the two ferromagnetic states $|\uparrow\rangle|\uparrow\rangle$ or $|\downarrow\rangle|\downarrow\rangle$. While approaching the transition, there can be oscillation only between these two states, and after the transition, the qubits can only be in one of the two states. As we demonstrated in the

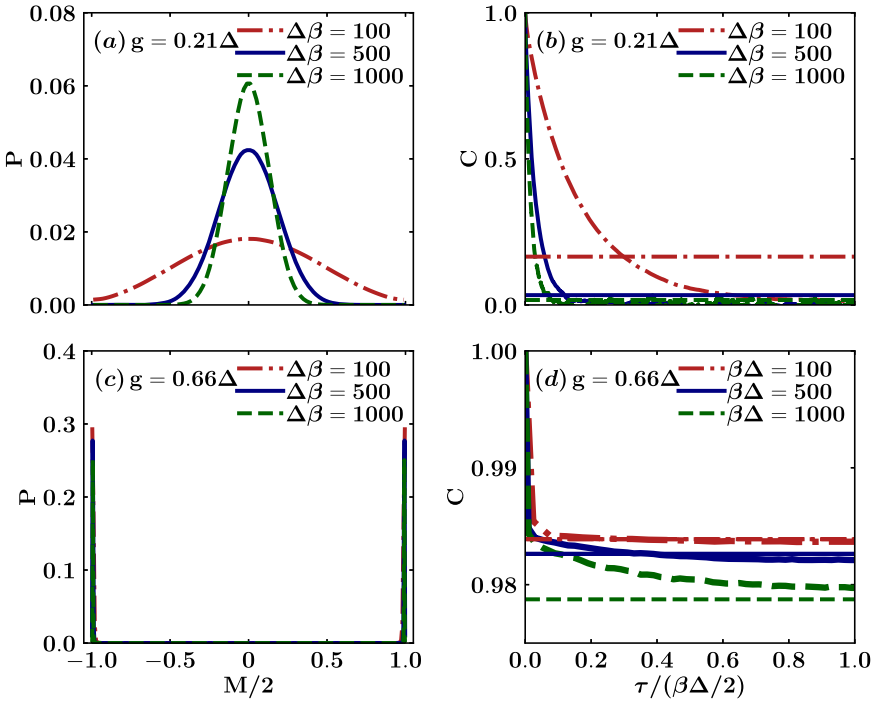

Fig. 4 | Bimodal magnetization distribution and correlations signal the QPT at thermodynamic equilibrium. Qubits' magnetization distribution $P(M/2)$ ((**a**) and (**c**)) and normalized correlation function $C = C(\tau/(\beta\Delta/2))/C(0)$ ((**b**) and (**d**)). We consider two scenarios: one with $g = 0.21\Delta$ before the transition ((**a**) and (**b**)) and another with $g = 0.66\Delta$ after the transition ((**c**) and (**d**)). These calculations are performed using the WLMC method at inverse temperatures of $\beta\Delta \in [100, 1000]$.

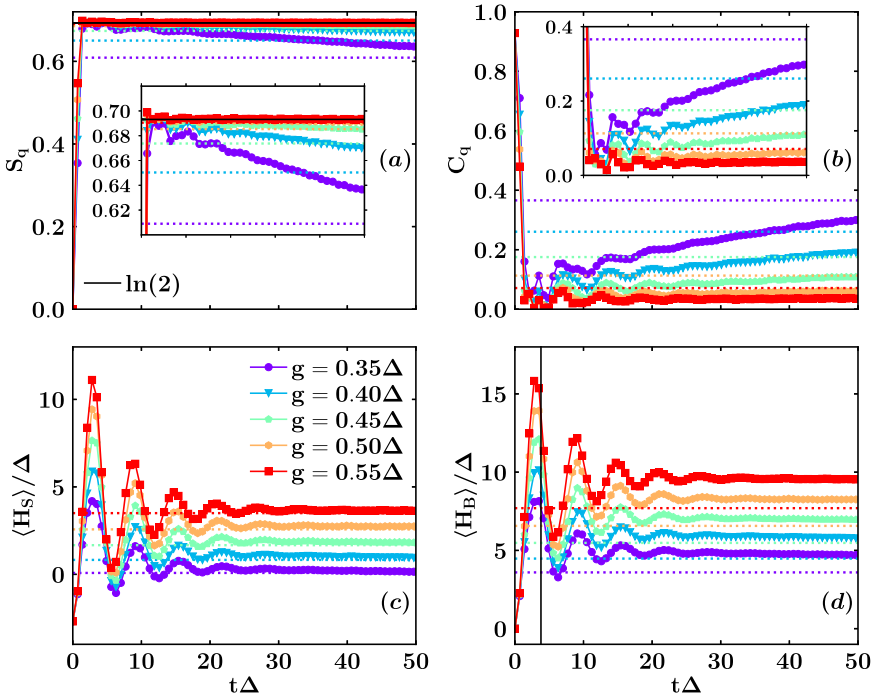

Fig. 5 | Energy and entanglement dynamical behavior. Qubits' entropy S_q (**a**) and concurrence C_q (**b**), system energy $\langle H_S(t)\rangle/\Delta$ (**c**) and bath energy $\langle H_B(t)\rangle/\Delta$ (**d**) as functions of dimensionless time $t\Delta$ for different values of the coupling $g \in [0.35, 0.55]\Delta$ and $J = -10\Delta$, crossing the critical point, calculated through TDVP and DMRG. The insets in panels (**a**) and (**b**) provide a zoomed-in view of the long-time behaviors. The dotted lines represent the DMRG equilibrium values corresponding to the TDVP dynamical values, shown as solid lines with markers specified in the legend. In panel (**a**), the horizontal black line indicates the maximum value of von Neumann entropy for a single qubit. In panel (**d**), the vertical black line marks the critical time at which the DQPT occurs.

Supplemental Material of ref. 5, one can adiabatically apply a magnetic field on the qubits or an electric field on the oscillator and examine the response function of the qubits or the oscillator, respectively. Observing the system after the critical coupling, where the equilibrium transition occurs, reveals that the system no longer relaxes and becomes localized. This is described in Supplementary Note 2 and illustrated by the oscillator relaxation function Σ_x in Supplementary Fig. 2, which remains constant at 1 (indicating no relaxation) after the transition. This also suggests that one can look at the oscillator, which is sensitive to the change of the quench parameter g, and it monitors the behavior of the qubits in the localization transition. Therefore, the oscillator could be useful for measuring qubits and has potential applications in quantum sensing.

The results discussed above can be understood by examining the mapped model. The effective kernel for asymptotic imaginary times (low-frequency regime) is linear in the frequency, as in the case of the Ohmic bath of a single spin-boson model. This low-frequency behavior implies an asymptotic $1/\tau^2$ behavior that is the fingerprint of a delocalized-localized transition, observable by increasing the effective coupling. In the Rabi model, this effective coupling depends not only on the bath coupling already present in the spin-boson model but also on the coupling g and the oscillator frequency ω_0.

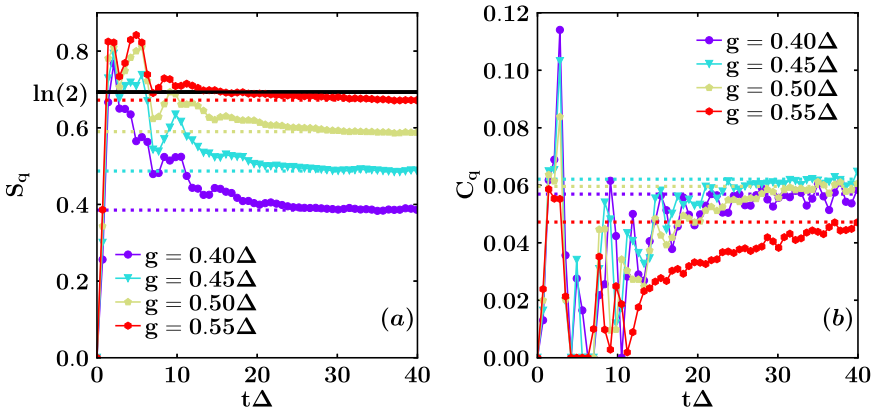

Fig. 6 | Entanglement dynamical behavior. Qubits' entropy S_q (**a**) and concurrence C_q (**b**) as functions of dimensionless time $t\Delta$ for different values of the coupling $g \in [0.40, 0.55]\Delta$ and $J = 0$, near the critical point, computed through TDVP and DMRG. The dotted lines represent the DMRG equilibrium values corresponding to the TDVP dynamical values, shown as solid lines with markers specified in the legend. In panel (**a**), the horizontal black line indicates the maximum value of von Neumann entropy for a single qubit.

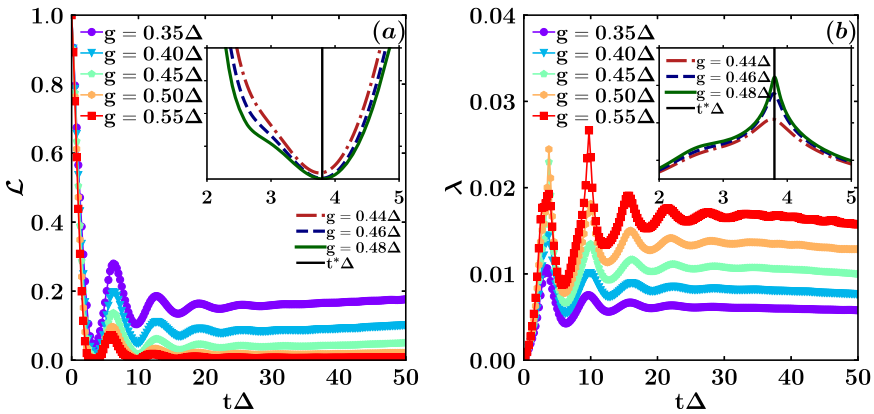

Fig. 7 | Non-analytical behavior of Loschmidt echo's rate function signals DQPTs. Loschmidt echo $\mathcal{L}(t)$ (**a**) and rate function $\lambda(t)$ (**b**) as functions of dimensionless time $t\Delta$ for different values of the coupling $g \in [0.35, 0.55]\Delta$ and $J = -10\Delta$, crossing the critical point, computed through TDVP. The insets provide a zoomed-in view near the transition, allowing identifying the critical time $t^*\Delta \approx 3.8$.

Regarding energy contributions, as depicted in Fig. 5c, the mean value of the system's energy $\langle H_S(t)\rangle$ approaches its thermodynamic equilibrium value after approximately $t\Delta = 30$, while the mean value of the bath energy $\langle H_B(t)\rangle$ (see Fig. 5d) never reaches the DMRG values. We also computed the mean value of the interaction energy $\langle H_{S-B}(t)\rangle$, although it is not shown here, which reaches thermodynamic equilibrium on the same time scale as the system. The total energy is conserved, the bath remains at zero temperature, but accumulating bosons, i.e., absorbing the energy difference relative to the ground-state energy calculated through DMRG. This phenomenon can also be understood in terms of quasiparticles. When the coupling g is small, the system reaches the equilibrium of its Hamiltonian H_S. However, as g increases, one can envision another Hamiltonian involving non-interacting quasiparticles dressed by the bath bosons, resulting in a small residual interaction energy. Consequently, quasiparticles reach the thermodynamic equilibrium in the presence of additive free bosons that are not able to modify the bath temperature. After analyzing asymptotic times, in the following we will focus our attention on smaller time scales.

We again study the out-of-equilibrium properties in the case of $J = 0$, comparing long-times dynamics with thermodynamic equilibrium. Specifically, we calculate the qubits' entropy $S_q(t)$, and the concurrence $C_q(t)$ for different values of g, approaching the critical point. In Fig. 6a, b, we can see that both entropy and entanglement approach their thermodynamic values at earlier times than in the $J \neq 0$ case. To quantitatively understand the approach to equilibrium for these quantities, we also fitted the curves for the two values of J. This confirmed that the decay of the entropy and the saturation of the concurrence have already reached the long times necessary to observe equilibrium observables for $J = 0$. In contrast, for $J \neq 0$, we need a time on the order of $t\Delta \approx 10^3$, which is too difficult to achieve numerically. Moreover, the greater the value of g, the more time the system needs to reach equilibrium values. This very long-time equilibration can be explained physically by noting that when $J = 0$, the system is directly connected to the bath, making it easier to reach thermodynamic equilibrium. In contrast, in the case of $J = -10\Delta$, the very strong qubit-qubit interaction complicates the interplay between the internal dynamics and the equilibration process, leading to thermodynamic equilibrium being reached over much longer times.

We do not show the time behavior of the energy contributions, but we have analyzed them, finding results similar to the interacting case. That is, the system's energy and the interaction with the bath approach equilibrium values, while the bath's energy remains different, accounting for the overall difference in energy due to the initial excited state.

Dynamical quantum phase transitions: Loschmidt echo

It has been demonstrated in refs. 7,8 that a closed quantum many-body system can undergo a DQPT without any external control parameters, such as temperature or pressure. The typical non-analyticities of phase transitions manifest over time in the matrix element of the system unitary evolution operator on the initial state, i.e., the Loschmidt echo $\mathcal{L}(t)$ (see Fig. 7a). To observe such a phase transition, the procedure involves preparing the system in a well determined initial state inducing a quench in a parameter on which the Hamiltonian depends. Subsequently, the system evolves with the full Hamiltonian after the quench, and the Loschmidt echo is computed over time[48]. It can be expressed as $\mathcal{L}(t) = e^{-N\lambda(t)}$ taking into account the exponential dependence on the system's degrees of freedom, denoted by N. Therefore, the rate function $\lambda(t)$ (see Fig. 7b) is the key property to monitor over time in order to observe non-analyticities. Formally, there exists an equivalence between the rate function and the free energy derived from a complex partition function, demonstrating the presence of singular points. Here, we aim to compute the same quantities in the closed system, which includes the bath. We underline that we operate with the entire system energy fixed in an excited state[7], whereas the QPT is studied using WLMC and DMRG, which examine the entire system's ground state. Consequently,

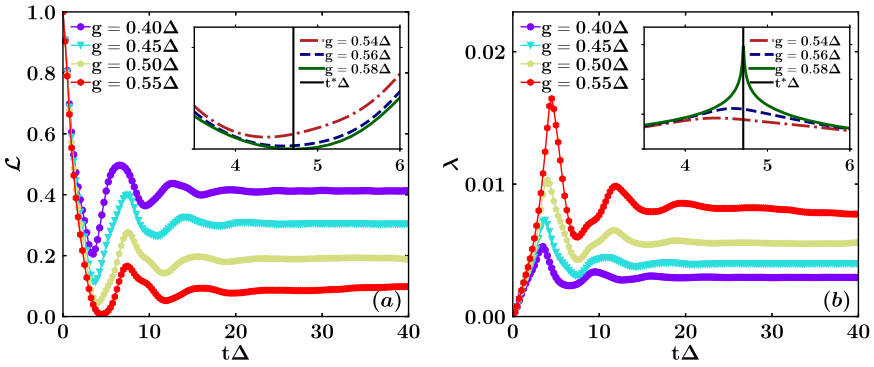

Fig. 8 | Non-analytical behavior of Loschmidt echo's rate function signals DQPTs. Loschmidt echo $\mathcal{L}(t)$ (**a**) and rate function $\lambda(t)$ (**b**) as functions of dimensionless time $t\Delta$ for different values of the coupling $g \in [0.40, 0.55]\Delta$ and $J = 0$, near the critical point, computed through TDVP. The insets provide a zoomed-in view near the transition allowing to identify the critical time $t^*\Delta \approx 4.7$.

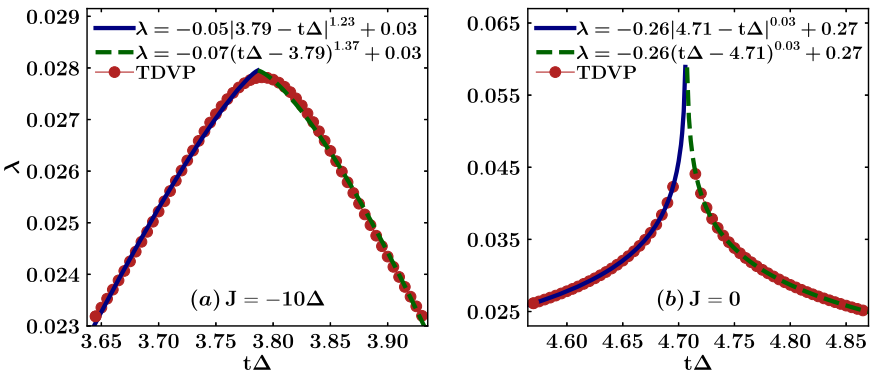

Fig. 9 | Critical exponent of non-analicities of Loschmidt echo's rate function to classify DQPTs. Loschmidt echo rate function $\lambda(t)$ as functions of dimensionless time $t\Delta$ for the two cases $J = -10\Delta, g = 0.48\Delta$ (**a**) and $J = 0$, $g = 0.58\Delta$ (**b**). The red points represent data computed through TDVP. For each case, we provide fitting functions for both the left branch (blue solid line) and the right branch (green dashed line). The legend indicates the parameter values obtained from the fit.

the dynamical behavior we observe is due to energy fluctuations above the ground state; therefore, we cannot expect the two transitions to occur at exactly the same parameter values.

Figure 7 illustrates the echo and the rate function over time for different values of g around the transition. Additionally, the inset clearly demonstrates how the scalar product between the evolved state and the initial one becomes zero (see inset of Fig. 7a) and the kink becomes narrower and higher as the critical point is approached at time $t^*\Delta \approx 3.8$ (see inset of Fig. 7b). In Fig. 5d we can see that the first maximum at short times occurs at around the critical time indicated by the black vertical line, as another marker of the transition in the dynamics. Beyond the critical region, the peak occurs at earlier times, and multiple peaks emerge over time in the rate function. This behavior occurs because the system can transition to the other phase more rapidly with higher couplings to the bath. The scalar product which vanishes indicates that the bath, including a lot of excited bosons, significantly differs from the initial vacuum state, leading to the orthogonality catastrophe, a characteristic feature of a phase transition. We emphasize that, through the quench, we are probing the first excited states and fluctuations are responsible for the observation of the DQPTs, reminiscent of the QPT occurring at thermodynamic equilibrium at zero temperature in the ground state of the entire Hamiltonian. In the Supplementary Note 3, we demonstrate that the two-qubit subsystem does not transition by computing the fidelity between the evolved state and the initial one. This fidelity coincides with the open systems generalization described in[11], given that our initial state is pure. As shown in Supplementary Fig. 3, it does not vanish over time and hence its logarithm does not exhibit non-analyticities. This confirms the idea that the phenomenon we are observing is a dissipation driven DQPT.

We again present the Loschmidt echo and the corresponding rate function over time for the non-interacting qubits case. Figure 8 shows the echo and the rate function for different values of g near the transition. As in the previous case, the inset in Fig. 8a clearly shows how the scalar product between the evolved state and the initial state drops to zero as the kink becomes narrower and higher, especially near the critical point at $t^*\Delta \approx 4.7$ (see the inset of Fig. 8b). Beyond the critical value $g_c \approx 0.6\Delta$, the peak appears at earlier times, and multiple peaks emerge over time in the rate function. As with the interacting case, energy fluctuations might account for the observation of the DQPT in the excited states, resembling the QPT seen at thermodynamic equilibrium at zero temperature in the ground state of the entire Hamiltonian.

To further classify the DQPTs, we study the critical exponent of the rate function of the Loschmidt echo, focusing on the $J = -10\Delta$ case and the $J = 0$ case. The corresponding results are presented in Fig. 9a, b, respectively. We fit the left branch of the data, preceding the peaks, using the function $\lambda(t) = a_L|d_L - t|^{b_L} + c_L$ with four free parameters. Subsequently, we fix d_L and c_L, the coordinates of the peak, for the right branch fitting, which employs the function $\lambda(t) = a_R(t - d_L)^{b_R} + c_L$ with two free parameters. In the fit performed for the $J = 0$ case, we exclude the central points next to the peak.

Our analysis reveals that in the case of $J = -10\Delta$, the critical exponent b is approximately 1 for both branches. However, in the $J = 0$ case, the critical exponent b exhibits significantly different behavior, being on the order of 0.03 for both branches. These distinct behaviors point out the significant impact of interactions and entanglement.

As detailed in the Methods Sec. Worldline Monte Carlo method, our model can be mapped by eliminating structured bath degrees of freedom. The resulting effective Euclidean action is characterized by a spin-boson model extended to involve two qubits interacting with the bath, yielding a classical system of spin variables distributed along chains of length β with long-range ferromagnetic interactions. The additional interaction between the two qubits, governed by J, induces short-range interactions between the spin chains. From this perspective, we interpret our resulting critical exponents in analogy with other studies focusing on Ising spin chains and the occurrence of DQPTs. In particular, the case of $J = -10\Delta$ can be seen as a system where the short-range interaction between the two chains and the initial qubits' entanglement are dominant for short times, inducing a quasi-

linear critical exponent similar to those observed in short-range Ising chains[20]. In the $J = 0$ case, only long-range ferromagnetic interactions are present, with no entanglement between qubits. Interactions between the chains are induced by the coupling to the bath, reducing the critical exponent. As mentioned in the introduction, it has been shown[21] that long-range interactions can give rise to DQPTs. However, the exact value of the critical exponent in our case with $\gamma = 2$ (BKT), given γ defined by the $1/r^{\gamma}$ behavior for long-range interactions, remains unclear. Additionally[23], demonstrates that one can obtain a non-linear singularity by changing some parameters in the quench, and[22] effectively reduces the critical exponent by considering a random Ising chain.

Discussion

We emphasize that, unlike the model in ref. 49, which considers a more general interaction between the qubits but omits interaction with the bath, our model explicitly incorporates dissipation. Additionally, the absence of transverse coupling to the oscillator in ref. 49 allows for the decoupling of two degenerate solutions. Since our focus is on dynamical transitions induced by the environment, we treat the bath and the two-qubit-oscillator system on equal footing across all coupling regimes, overcoming the limitations of the perturbative Lindblad approach[50].

We note that the same signatures of the BKT QPT at thermodynamic equilibrium, as identified in ref. 5, are observed in the two-qubit system. We then focus on the bimodal magnetization distribution and entanglement properties. Moreover, we investigate the effects of short- and long-range interactions, which are crucial in our model, leading to distinct DQPTs that are not achievable in the model discussed in ref. 5.

While we employ some of the same numerical techniques as in previous work, this study focuses on dynamical transitions and behavior, rather than just the relaxation processes tied to equilibrium transitions, which was the primary dynamical analysis in our earlier study. Finally, we emphasize that although the relationship between QPTs and DQPTs remains generally unclear, our study observes both types of transitions within a specific parameter range.

Conclusions

We have shown that an interacting two-qubit model strongly coupled to a $T = 0$ bath exhibits dynamical phase transitions not present in the closed configuration (no coupling with the bath). We also provide evidence that the DQPTs are related to a BKT equilibrium QPT. Our analysis not only encompasses the investigation of singularities in the rate function but also highlights clear signatures of the DQPT through entanglement properties, such as the qubits' von Neumann entropy and concurrence. Additionally, we observe the impact of interaction by examining the critical exponent of the singularities in the Loschmidt echo rate function for both the interacting ($J = -10\Delta$) and non-interacting ($J = 0$) cases. We find two classes of emergent dynamical critical phenomena demonstrating a shift from exponent 1 in the former case to 0.03 in the latter, attributed to the different role of entanglement dynamics.

Our findings challenge the conventional belief that the environment invariably exerts a detrimental influence on the DQPT of the system. Instead, we reveal that the environment can induce dynamical phase transitions. These results pave the way for experimental investigations. Indeed, recent advancements in quantum technologies, such as superconducting qubits and circuit QED setups, make feasible the experimental realization of our proposed model and the observation of dynamical quantum phase transitions induced by the environment, opening up possibilities in quantum devices. Moreover, our study shows a criticality-enhanced sensitivity of the Loschmidt echo, which can be utilized in quantum sensing applications.

Methods

Equilibrium properties are explored using two distinct methods. Firstly, the WLMC approach, based on path integrals, eliminates the structured bath degrees of freedom, yielding an effective Euclidean action. The second approach, DMRG, utilizes an adaptive algorithm and MPS representation to determine ground state properties. For out-of-equilibrium properties, the TDVP algorithm is employed to evolve the wavefunction of the entire system, represented as an MPS.

Time-dependent variational principle numerical simulations

We employ time-dependent MPS simulations, implemented with ITensor Library[44], to investigate the system's dynamics, specifically focusing on energy and entanglement behaviors. We analyze the Loschmidt echo and the corresponding rate function. The long-range interactions between the oscillator, connected to the two qubits, and the bath modes are described using the star geometry. In this configuration, the qubits of frequency Δ are placed on the first two sites, the oscillator of frequency $\omega_0 = \Delta$ and Hilbert space dimension N_{osc} on the third one, and the collection of N bosonic modes of the bath with frequencies ω_i on the remaining sites. The couplings between the oscillator and each bosonic mode are defined to describe the bath in terms of an Ohmic spectral density.

The bath Hamiltonian from Eq. (2) in the main text can be expressed as follows:

$$H_B = \sum_{i=1}^{N}\left[\omega_i a_i^{\dagger}a_i + \frac{x_0^2}{2}M_i\omega_i^2\right] - (a + a^{\dagger})\sum_{i=1}^{N}|\lambda_i|(a_i + a_i^{\dagger}). \quad (3)$$

The coupling constants to the bath are $|\lambda_i| = \sqrt{\frac{k_i\omega_i}{4m\omega_0}}$. We neglect the energy shift $\sum_{i=1}^{N}\omega_i/2$, which does not affect the dynamics. Therefore, the Hamiltonian of the system plus the environment can be rewritten by defining a renormalized oscillator frequency $\bar{\omega}_0 = \sqrt{\omega_0^2 + \sum_{i=1}^{N}M_i\omega_i^2/m}$. This frequency ensures that the total energy is bounded from below, and the quadratic form is positive definite. In superconducting circuits, this is natural and leads to the quadratic correction of bosonic modes, ensuring that the resonance of the cavity does not change its value irrespective of the dissipation strength. We also define renormalized coupling strengths $\bar{g} = g\sqrt{\frac{\omega_0}{\bar{\omega}_0}}$ between the qubits and the oscillator, and $|\bar{g}_i| = \sqrt{\frac{k_i\omega_i}{4m\bar{\omega}_0}}$ between the oscillator and each bath bosonic mode. The total Hamiltonian in our MPS simulations is then given by:

$$\begin{aligned} H = &-\frac{\Delta}{2}\left(\sigma_x^1 + \sigma_x^2\right) + \frac{J}{4}\sigma_z^1\sigma_z^2 + \bar{g}\left(\sigma_z^1 + \sigma_z^2\right)(b + b^{\dagger}) \\ &+ \bar{\omega}_0 b^{\dagger}b + \sum_{i=1}^{N}\omega_i a_i^{\dagger}a_i - (b + b^{\dagger})\sum_{i=1}^{N}\left[|\bar{g}_i|(a_i + a_i^{\dagger})\right], \end{aligned} \quad (4)$$

where b, ($b^{\dagger}$) is the annihilation (creation) operator for the renormalized oscillator with frequency $\bar{\omega}_0$ and coordinates $\bar{x}_0 = \sqrt{\frac{1}{2m\bar{\omega}_0}}(b + b^{\dagger})$ and $\bar{p}_0 = i\sqrt{\frac{m\bar{\omega}_0}{2}}(b^{\dagger} - b)$. The bath is represented by an Ohmic spectral density: $J(\omega) = \sum_{i=1}^{N}|\bar{g}_i|^2\delta(\omega - \omega_i) = \frac{\alpha}{2}\omega\Theta(\omega_c - \omega)$, where ω_c is the cutoff frequency and $\Theta(x)$ is the Heaviside function. The dimensionless parameter α measures the strength of the oscillator-bath coupling.

We note that this model can be mapped[5,38,50] in such a way that, by including the oscillator as a further bosonic mode of the bath, the qubits are coupled to the $N + 1$ bath modes. We can define the couplings β_l between each qubit and each bosonic mode of frequency $\hat{\omega}_l$ and hence describe the bath in terms of an effective spectral density:

$$J_{\text{eff}}(\omega) = \sum_{l=1}^{N+1}|\beta_l|^2\delta(\omega - \hat{\omega}_l) \underset{N\to\infty}{\longrightarrow} \frac{2g^2\omega_0^2\alpha\omega}{(\omega^2 - \omega_0^2 - h(\omega))^2 + (\pi\alpha\omega_0\omega)^2}, \quad (5)$$

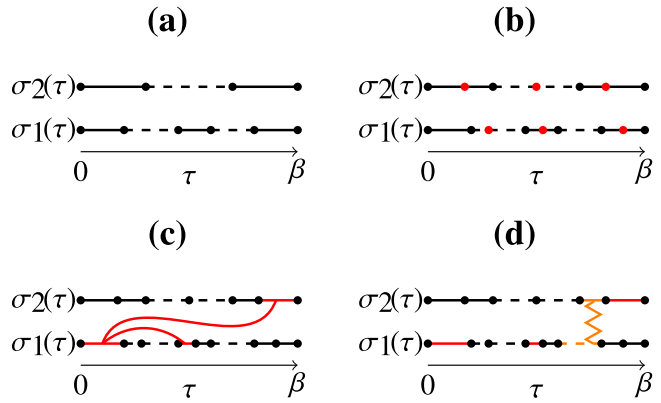

Fig. 10 | Worldline Monte Carlo updating scheme. The dashed lines are the $\sigma(\tau) = -1$ states, and the solid ones are the $\sigma(\tau) = 1$ states. The segments are called "super-spins". (**a**) Spin path configuration realization; (**b**) insert randomly, along the spin-paths, n new potential spin flips (red dots); (**c**) connect a random l super-spin to another m with probability $P_{add}(s_l^I, s_m^{II})$ (the red curved lines represent the long range ferromagnetic connection between the selected red solid segments); (**d**) connect a random l super-spin to another m with probability $P_{add}(s_l, s_m)$ (the orange zigzag lines represent the short-range antiferromagnetic connection between the selected orange segments, solid for σ_2 and dashed for σ_1).

where $h(\omega) = \alpha\omega_0\omega \log\left[\frac{\omega_c+\omega}{\omega_c-\omega}\right]$. The spectral density is Ohmic at low frequencies: $J_{\text{eff}}(\omega) \approx \frac{2g^2\alpha}{\omega_0^2}\omega$. Therefore, each qubit is coupled to the same oscillator bath through an effective constant proportional to $g^2\alpha/\omega_0^2$. This low-frequency behavior of the mapped model suggests the presence of the QPT. We study the system's dynamics for different values of the qubits-oscillator coupling g in the range $[0.0, 0.9]\Delta$, fixing $\alpha = 0.1$ and $\omega_c = 30\Delta$. We select the ground state of the Hamiltonian $H_S(g = 0)$ as the initial state for simulating the system's dynamics. We apply the TDVP[45–47], where the time-dependent Schrödinger equation is projected onto the tangent space of the MPS manifold with a fixed bond dimension at the current time.

In this study, we employ the two-site TDVP (2TDVP as described in ref. 47), using a second-order integrator with a left-right-left sweeping approach and a half-time step of $dt/2$. This method exhibits a time-step error of $O(dt^3)$, with accuracy controlled by the MPS bond dimension and the threshold to terminate the Krylov series. We halt the Krylov vectors recurrence when the total contribution of two consecutive vectors to the matrix exponential dropped below 10^{-12}. While more advanced methods, such as basis extension optimization[51,52], exist, we opt for convergence in the number of Fock states in the cavity ($N_{osc} = 16$) and bath modes ($N = 300$) with Hilbert space dimension ($N_{bos} = 3$). This approach allow us to find the optimal compromise between the smallest bond dimension and longest simulation times, by converging also over the time interval that we set to $dt\Delta = 0.01$.

Our truncation error remain below 10^{-13} by requiring a maximum bond dimension of $D_{max} = 50$. Simultaneously, this optimal maximum bond dimension enable us to achieve a final time for our simulations as large as $t_{final}\Delta = 50$.

Density-matrix renormalization group algorithm

We conduct an analysis of the equilibrium properties, namely energy and entanglement, for the entire system by computing its ground state through the DMRG algorithm. The results obtained using DMRG are compared with those acquired through the WLMC method. The model parameters are the same used for the TDVP simulations over time.

The DMRG algorithm[53–55] is an adaptive approach for optimizing an MPS, approximating the dominant eigenvector of a large matrix H, typically assumed to be Hermitian. This algorithm optimizes two neighboring MPS tensors iteratively, combining them into a single tensor for optimization. Techniques such as Lanczos or Davidson are employed for the optimization, followed by factorization using Singular Value Decomposition or density matrix decomposition. This process allows us to restore the MPS form and adapt the bond dimension during factorization, preserving the network's structure.

In our implementation of DMRG through the ITensor Library's dedicated function[44], we set several accuracy parameters. These include the maximum and minimum bond dimensions of any bond in the MPS, the truncation error cutoff during SVD or density matrix diagonalizations, the maximum number of Davidson iterations in the core DMRG step, and the magnitude of the noise term added to the density matrix to aid convergence. Convergence is achieved by ensuring that the final ground state energy returned after the DMRG calculation is within our specified numerical precision.

Worldline Monte Carlo method

WLMC is a path integral technique based on a Monte Carlo algorithm. Using the path integral formulation, it is possible to remove exactly all the phonon degrees of freedom of the thermal bath, obtaining the density matrix dependent only on the effective Euclidean action[32,40]

$$S = \frac{1}{2}\sum_{i,j}\int_0^\beta d\tau \int_0^\beta d\tau' \sigma_i(\tau) K_{\text{eff}}(\tau - \tau')\sigma_j(\tau'), \tag{6}$$

where the effective kernel is

$$K_{\text{eff}}(\tau) = \frac{1}{\pi}\int_0^\infty d\omega\, J_{\text{eff}}(\omega)\frac{\cosh(\omega(\beta/2 - \tau))}{\sinh(\omega\beta\tau)}, \tag{7}$$

with spectral density

$$J_{\text{eff}}(\omega) = \frac{2g^2\omega_0^2\alpha\omega}{(\omega^2 - \omega_0^2 - h(\omega))^2 + (\pi\alpha\omega_0\omega)^2}\Theta(\omega - \omega_c), \tag{8}$$

in which $h(\omega) = \alpha\omega_0\omega \log\left[\frac{\omega_c+\omega}{\omega_c-\omega}\right]$. We emphasize that this has the same form as derived in Eq. (5). Consequently, our simulations are conducted on the mapped system consisting of two qubits interacting with each other and with an effective bath. This scenario resembles that of a quantum Rabi model but is extended to involve two qubits. The problem is therefore equivalent, in the general multi-spin case, to a 2D system in which one dimension is discrete (that of the sites) and one is continuous of length β. The effective interaction due to K_{eff} consists of a long-range ferromagnetic interaction between the τ and τ' points of the worldlines. Between the sites at first neighbours along the discrete dimension (in the case of the studied model) the interaction is antiferromagnetic. The time cluster[40,42] algorithm used is based on an alternation of Wolff[43] and Metropolis moves: in the first step, as schematised in Fig. 10, we start with a worldline $\sigma_z(\tau)$ and add a number of potential spin flips extracted from a Poissonian distribution with mean $\beta\Delta/2$

$$P(n) = \frac{\mu^n}{n!}e^{-\mu}, \tag{9}$$

where $n = 0, 1, 2, \ldots$ and $\mu = \beta\Delta/2$. Then two of the new segments (having a real spin-flip point and a potential point as extremes) are randomly selected, with extremes u_1, u_2 and u_3, u_4. The connection of the two segments occurs with probability

$$P_{add}(s_l^I, s_m^{II}) = 1 - \exp\left\{\min\left[0, -2\int_{u_1}^{u_2} d\tau \int_{u_3}^{u_4} d\tau' s_l^I K_\beta(\tau - \tau') s_m^{II}\right]\right\}. \tag{10}$$

This step is iterated connecting the second segment to another randomly selected one. The process is iterated until no more segments are added to the cluster. The cluster is subsequently flipped with probability 1/2 and the potential spin flips introduced at the beginning that do not represent real flips are removed. The same procedure is carried out for the antiferromagnetic interaction at first neighbours by connecting segments along worldlines of opposite sign, of extremes u_1', u_2' and u_3', u_4', with probability

$$P_{add}(s_l, s_m) = 1 - \exp\{\min[0, 4\beta J s_l s_m]\}. \quad (11)$$

The rest of the algorithm is similar to the previous case. Finally, a Metropolis step is performed in which a segment is randomly selected and flipped, thus removing the extreme points that define the spin flips. We emphasise that this approach is exact from a numerical point of view, and it is equivalent to the sum of all the Feynman diagrams.

Data availability

All relevant data presented in the plots are available from the authors upon request to the corresponding author.

Received: 18 May 2024; Accepted: 28 October 2024;
Published online: 07 November 2024

References

1. Sachdev, S. https://doi.org/10.1017/CBO9780511973765 *Quantum Phase Transitions*, 2nd ed. (Cambridge University Press, 2011)
2. Schiró, M. & Fabrizio, M. Time-dependent mean field theory for quench dynamics in correlated electron systems. *Phys. Rev. Lett.* **105**, 076401 (2010).
3. Sciolla, B. & Biroli, G. Quantum quenches and off-equilibrium dynamical transition in the infinite-dimensional Bose-Hubbard model. *Phys. Rev. Lett.* **105**, 220401 (2010).
4. Hwang, M.-J., Rabl, P. & Plenio, M. B. Dissipative phase transition in the open quantum Rabi model. *Phys. Rev. A* **97**, 013825 (2018).
5. De Filippis, G. et al. Signatures of dissipation driven quantum phase transition in Rabi model. *Phys. Rev. Lett.* **130**, 210404 (2023).
6. Heyl, M., Polkovnikov, A. & Kehrein, S. Dynamical quantum phase transitions in the transverse-field ising model. *Phys. Rev. Lett.* **110**, 135704 (2013).
7. Heyl, M. Dynamical quantum phase transitions: a review. *Rep. Prog. Phys.* **81**, 054001 (2018).
8. Heyl, M. Dynamical quantum phase transitions: A brief survey. *Europhys. Lett.* **125**, 26001 (2019).
9. Zvyagin, A. A. Dynamical quantum phase transitions. *Low Temp. Phys.* **42**, 971 (2016).
10. Puebla, R. Finite-component dynamical quantum phase transitions. *Phys. Rev. B* **102**, 220302 (2020).
11. Link, V. & Strunz, W. T. Dynamical phase transitions in dissipative quantum dynamics with quantum optical realization. *Phys. Rev. Lett.* **125**, 143602 (2020).
12. Nava, A., Perroni, C. A., Egger, R., Lepori, L. & Giuliano, D. Lindblad master equation approach to the dissipative quench dynamics of planar superconductors. *Phys. Rev. B* **108**, 245129 (2023).
13. Nava, A., Perroni, C. A., Egger, R., Lepori, L. & Giuliano, D. Dissipation-driven dynamical topological phase transitions in two-dimensional superconductors. *Phys. Rev. B* **109**, L041107 (2024).
14. Dolgitzer, D., Zeng, D. & Chen, Y. Dynamical quantum phase transitions in the spin-boson model. *Opt. Express* **29**, 23988 (2021).
15. Nielsen, M. A. & Chuang, I. L., *Quantum computation and quantum information* (Cambridge university press, 2010)
16. Di Bello, G., De Filippis, G., Hamma, A. & Perroni, C. A. Optimal encoding of two dissipative interacting qubits. *Phys. Rev. B* **109**, 014304 (2024).
17. Osterloh, A., Amico, L., Falci, G. & Fazio, R. Scaling of entanglement close to a quantum phase transition. *Nat.* **416**, 608 (2002).
18. Canovi, E., Ercolessi, E., Naldesi, P., Taddia, L. & Vodola, D. Dynamics of entanglement entropy and entanglement spectrum crossing a quantum phase transition. *Phys. Rev. B* **89**, 104303 (2014).
19. De Nicola, S., Michailidis, A. A. & Serbyn, M. Entanglement view of dynamical quantum phase transitions. *Phys. Rev. Lett.* **126**, 040602 (2021).
20. Heyl, M. Scaling and universality at dynamical quantum phase transitions. *Phys. Rev. Lett.* **115**, 140602 (2015).
21. Žunkovič, B., Heyl, M., Knap, M. & Silva, A. Dynamical quantum phase transitions in spin chains with long-range interactions: Merging different concepts of nonequilibrium criticality. *Phys. Rev. Lett.* **120**, 130601 (2018).
22. Trapin, D., Halimeh, J. C. & Heyl, M. Unconventional critical exponents at dynamical quantum phase transitions in a random ising chain. *Phys. Rev. B* **104**, 115159 (2021).
23. Wu, Y. Dynamical quantum phase transitions of quantum spin chains with a loschmidt-rate critical exponent equal to 1 2. *Phys. Rev. B* **101**, 064427 (2020).
24. Chu, Y., Zhang, S., Yu, B. & Cai, J. Dynamic framework for criticality-enhanced quantum sensing. *Physical Review Letters* **126**, 010502 (2021).
25. Lü, J.-H. et al. Critical quantum sensing based on the jaynes-cummings model with a squeezing drive. *Physical Review A* **106**, 062616 (2022).
26. Ying, Z.-J., Felicetti, S., Liu, G. & Braak, D. Critical quantum metrology in the non-linear quantum rabi model. *Entropy* **24**, 1015 (2022).
27. Langfitt, Q., Saleem, Z. H., Zhong, T., Shaji, A. & Gray, S. K. https://arxiv.org/abs/2312.04766. Enhanced quantum sensing mediated by a cavity in open systems (2023).
28. Ding, D.-S. et al. Enhanced metrology at the critical point of a many-body rydberg atomic system. *Nature Physics* **18**, 1447 (2022).
29. De Filippis, G. et al. Quantum phase transitions in the spin-boson model: Monte carlo method versus variational approach à la feynman. *Phys. Rev. B* **101**, 180408 (2020).
30. Schuler, M., De Bernardis, D., Läuchli, A. & Rabl, P. The vacua of dipolar cavity quantum electrodynamics. *SciPost Physics* **9**, 066 (2020).
31. Caldeira, A. O. & Leggett, A. J. Influence of dissipation on quantum tunneling in macroscopic systems. *Phys. Rev. Lett.* **46**, 211 (1981).
32. Weiss, U., *Quantum dissipative systems* (World Scientific, 2012)
33. Kozin, V. K., Miserev, D., Loss, D. & Klinovaja, J. Quantum phase transitions and cat states in cavity-coupled quantum dots. *Phys. Rev. Res.* **6**, 033188 (2024).
34. Magazzù, L. & Grifoni, M. Transmission spectra of an ultrastrongly coupled qubit-dissipative resonator system. *J. Stat. Mech. Theory Exp.* **2019**, 104002 (2019).
35. Goorden, M., Thorwart, M. & Grifoni, M. Entanglement spectroscopy of a driven solid-state qubit and its detector. *Phys. Rev. Lett.* **93**, 267005 (2004).
36. Malekakhlagh, M. & Rodriguez, A. W. Quantum Rabi model with two-photon relaxation. *Phys. Rev. Lett.* **122**, 043601 (2019).
37. Cai, M.-L. et al. Observation of a quantum phase transition in the quantum Rabi model with a single trapped ion. *Nat. Commun.* **12**, 1126 (2021).
38. Zueco, D., Reuther, G. M., Kohler, S. & Hänggi, P. Qubit-oscillator dynamics in the dispersive regime: Analytical theory beyond the rotating-wave approximation. *Phys. Rev. A* **80**, 033846 (2009).
39. De Filippis, G. et al. Quantum phase transition of many interacting spins coupled to a bosonic bath: Static and dynamical properties. *Phys. Rev. B* **104**, L060410 (2021).
40. Winter, A., Rieger, H., Vojta, M. & Bulla, R. Quantum phase transition in the sub-ohmic spin-boson model: Quantum monte carlo study with a continuous imaginary time cluster algorithm. *Phys. Rev. Lett.* **102**, 030601 (2009).

41. Feynman, R. P. Mathematical formulation of the quantum theory of electromagnetic interaction. *Phys. Rev.* **80**, 440 (1950).
42. Rieger, H. & Kawashima, N. Application of a continuous time cluster algorithm to the two-dimensional random quantum ising ferromagnet. *Eur. Phys. J. B Condens. Matter* **9**, 233 (1999).
43. Wolff, U. Collective monte carlo updating for spin systems. *Phys. Rev. Lett.* **62**, 361 (1989).
44. Fishman, M., White, S. & Stoudenmire, E. The itensor software library for tensor network calculations, SciPost Physics Codebases, 004 (2022).
45. Haegeman, J. et al. Time-dependent variational principle for quantum lattices. *Phys. Rev. Lett.* **107**, 070601 (2011).
46. Haegeman, J., Lubich, C., Oseledets, I., Vandereycken, B. & Verstraete, F. Unifying time evolution and optimization with matrix product states. *Phys. Rev. B* **94**, 165116 (2016).
47. Paeckel, S. et al. Time-evolution methods for matrix-product states. *Ann. Phys.* **411**, 167998 (2019).
48. Medvidović, M. & Sels, D. Variational quantum dynamics of two-dimensional rotor models. *PRX Quantum* **4**, 040302 (2023).
49. Grimaudo, R., de Castro, A. M., Messina, A., Solano, E. & Valenti, D. Quantum phase transitions for an integrable quantum Rabi-like model with two interacting qubits. *Phys. Rev. Lett.* **130**, 043602 (2023).
50. Di Bello, G. et al. Qubit-oscillator relationships in the open quantum Rabi model: the role of dissipation. *Eur. Phys. J. Plus* **138**, 135 (2023).
51. Zhang, C., Jeckelmann, E. & White, S. R. Density matrix approach to local hilbert space reduction. *Phys. Rev. Lett.* **80**, 2661 (1998).
52. Brockt, C., Dorfner, F., Vidmar, L., Heidrich-Meisner, F. & Jeckelmann, E. Matrix-product-state method with a dynamical local basis optimization for bosonic systems out of equilibrium. *Phys. Rev. B* **92**, 241106 (2015).
53. White, S. R. Density matrix formulation for quantum renormalization groups. *Phys. Rev. Lett.* **69**, 2863 (1992).
54. Schollwöck, U. The density-matrix renormalization group. *Rev. Mod. Phys.* **77**, 259 (2005).
55. Schollwöck, U. The density-matrix renormalization group in the age of matrix product states. *Ann. Phys.* **326**, 96 (2011).

Acknowledgements

G.D.F. acknowledges financial support from 376 PNRR MUR Project No. PE0000023-NQSTI. C.A.P. acknowledges founding from the European Union's Horizon Europe research and innovation programme under grant agreement n. 101115190. G.D.F. and C.A.P. acknowledge founding from the PRIN 2022 project 2022FLSPAJ "Taming Noisy Quantum Dynamics" (TANQU). C.A.P. acknowledges founding from the PRIN 2022 PNRR project P2022SB73K - "Superconductivity in KTaO3 Oxide-2DEG NAnodevices for Topological quantum Applications" (SONATA) financed by the European Union - Next Generation EU.

Author contributions

G.D.B. wrote the code and ran the numerical MPS simulations. A.P. and A.d.C. wrote the code and ran the numerical WLMC simulations. F.P., V.C., G.D.F., and C.A.P. developed the complete theoretical framework. All authors discussed the results and contributed to writing the manuscript.

Competing interests

The authors declare no competing interests.

Additional information

Supplementary information The online version contains supplementary material available at https://doi.org/10.1038/s42005-024-01855-8.

Correspondence and requests for materials should be addressed to Grazia Di Bello.

Peer review information *Communications Physics* thanks the anonymous reviewers for their contribution to the peer review of this work.